

PHASE-SPECIFIC SEMI-EMPIRICAL AEROACOUSTIC NOISE MODELING OF A CARGO eVTOL UAV WITH CONSIDERATION OF A SIMPLIFIED URBAN FLYOVER CASE

Illia Peleshok[1] & Mirko Hornung[1]

[1]Chair of Aircraft Design, Technical University of Munich, TUM School of Engineering and Design, Department of Aerospace and Geodesy, Boltzmannstrasse 15, 85748 Garching, Germany.

Abstract

For the operation of Unmanned Aerial Vehicles (UAVs) in urban environments, noise emitted by the UAV and the resulting noise exposure for the population are important aspects that must be considered. To increase public acceptance of UAV operations, noise models are required to assess and estimate UAV noise emissions. In this paper, flight-phase-specific semi-empirical noise source models for a cargo UAV are presented, each derived from selected noise-measurement segments of a complete flight mission. In addition, a measurement campaign simulating a simple urban flyover case was conducted, and a preliminary receiver-side wall-extension approach is investigated. These models are intended to support phase-specific UAV noise emission modeling and provide a basis for future mission-level applications.

Keywords: eVTOL, UAV, aeroacoustics, semi-empirical noise model, flight test data

1. Introduction

As Urban Air Mobility (UAM) continues to develop, noise emissions caused by Unmanned Aerial Vehicles (UAV) operations represent one of the key factors influencing public acceptance [1]. In order to understand and reduce the noise exposure of the population, appropriate methods for noise assessment and management are required [2]. For this purpose, aeroacoustic models are needed to estimate UAV noise emissions along representative flight missions. Such models can support UAV operations in urban areas by enabling mission planning with respect to noise emissions.

Previous studies have shown that drone noise perception and annoyance depend on drone size, flight maneuver and operating speed [3]. This indicates that the acoustic behavior of a UAV should be considered in relation to its operating condition rather than by a single stationary source description.

Measurement-based semi-empirical modeling provides one possible way to describe such operating-condition-dependent UAV noise emissions. The modeling approach used in the present work builds on the concept of flight-test-based system identification and compact semi-empirical source modeling developed at Technical University of Munich, Chair of Aircraft Design (TUM LLS) [4], [5]. In the present study, this approach is applied in a phase-specific manner to account for the different operating conditions encountered during the mission. Related work on multicopter noise modeling has also shown that measurement-based source models can include directivity and operating-condition effects, for example through procedure- or forward-flight-related correction terms [6].

However, free-field source models do not include reflections of acoustic waves, for example from buildings, which are expected to influence acoustic exposure in urban environments, particularly for cargo UAV flyover scenarios where reflective surfaces are present along the flight path. Schäfer et al. [7] have shown that models restricted to direct sound and ground reflection are insufficient near residential structures, where reflections and diffraction at buildings should be considered.

In this work, a separated lift and cruise fixed-wing cargo UAV configuration is investigated using aeroacoustic in-flight measurements of a complete UAV mission. Since the UAV operates in different

flight phases, the present paper develops phase-specific semi-empirical source models for a cargo electric vertical take-off and landing (eVTOL) UAV mission and evaluates a preliminary near-wall extension of the cruise model for a simplified urban flyover case.

2. Experimental Setup and Flight Measurement Campaign

The UAV used for the aeroacoustic flight measurements is an experimental separated lift and cruise cargo UAV called PW.Orca, manufactured by Phoenix Wings. PW.Orca is designed for transporting goods such as medical supplies, a mission profile that may include operations in urban areas and therefore makes this UAV particularly relevant for the investigation of noise emissions and community noise perception. PW.Orca is equipped with six hover propellers for vertical take-off and landing, two propellers for cruise flight, as well as wings with a wingspan of 2.98 m for wing-borne flight and a cruise speed of up to 110 km/h [8]. Figure 1 shows the UAV and an example of the microphone arrangement at the flight test field.



Figure 1 – UAV PW.Orca and example of the microphone arrangement at the flight test field.

For the acoustic measurements, a mobile frontend decentralized measurement system Squadriga III manufactured by HEAD Acoustics and eight ½-inch free-field microphones were used. The measurement system is equipped with a Global Positioning System (GPS) sensor, enabling synchronization of the measurement data during post-processing using GPS timestamps.

The measurement campaign was conducted during summer at the Goldachfeld test field in the municipality of Ismaning, Germany. The microphone setup was selected such that as many UAV emission angles as possible could be captured by the microphones during all flight phases. To achieve this angular coverage, six microphones were arranged in a straight line perpendicular to the UAV flyover trajectory, with a spacing of 15 m between adjacent microphones. The microphones were mounted on circular metallic ground plates and tripods, following the general recommendations of the European Union Aviation Safety Agency (EASA) guidelines [9].

The measurements were conducted under stable weather conditions with no precipitation. Some parts of the measurements were contaminated by noise from commercial aircraft passing over the test field near Munich Airport (MUC). These data segments were excluded from the analysis.

The objective of the experiment was to measure the noise emissions of PW.Orca UAV during all flight phases. The flight mission consisted of vertical take-off, transition into cruise flight, cruise flight with ten flyovers above the microphone array, retransition into vertical landing, and the landing phase itself. The flight trajectory over the Goldachfeld test area and the microphone arrangement are shown in Figure 2.

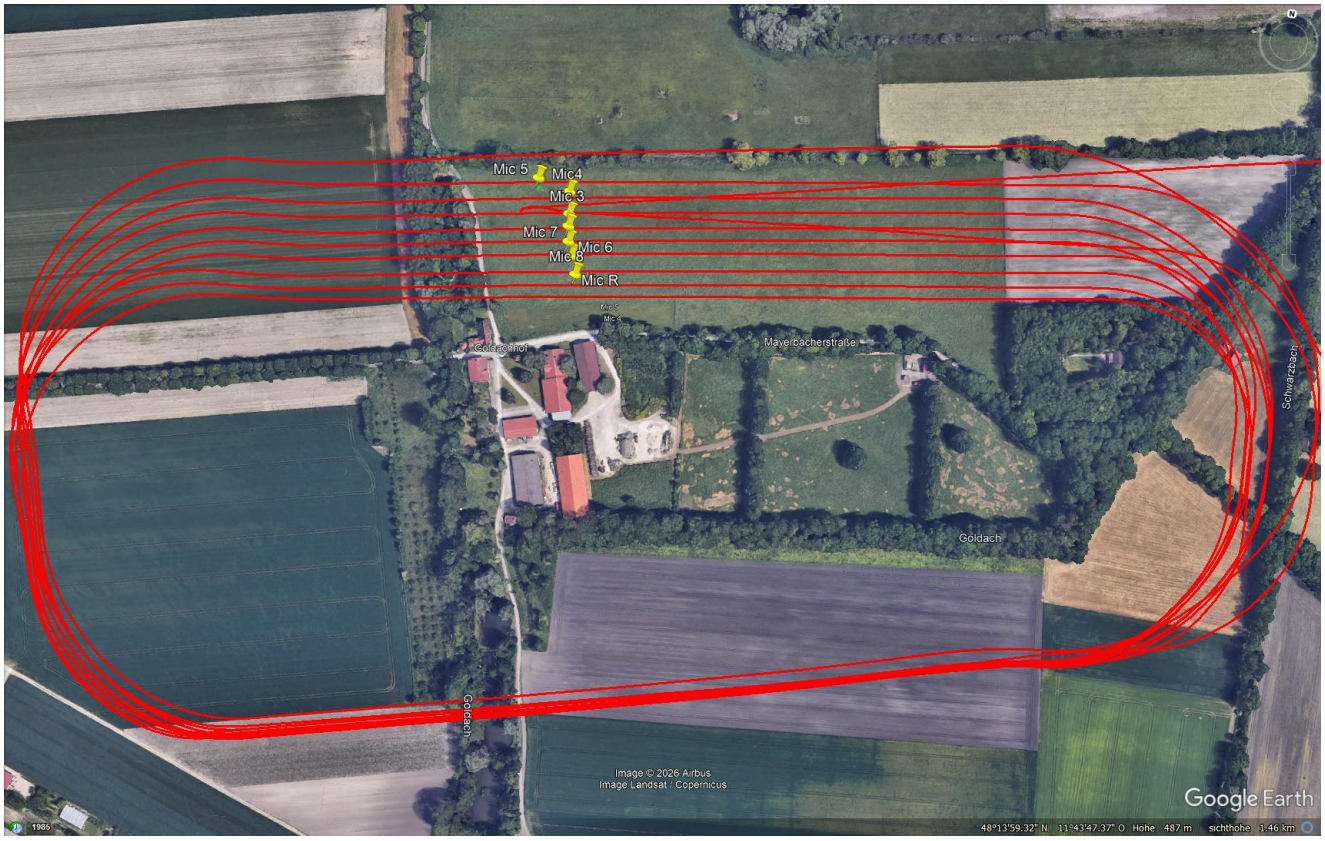


Figure 2 – UAV trajectory over the microphone array and arrangement of the microphones at the flight test field.

Additionally, a wall was installed at the flight test field in order to represent a simplified urban flyover case. This experimental setup is described in Section 5.

3. Acoustic Data Processing

The acoustic recordings obtained from the measurement system were first processed in the ArtemisSuite software environment. In this step, non-relevant parts of the recordings were removed to reduce computational effort, and acoustic quantities such as sound pressure level (SPL) and Fast Fourier transform (FFT) spectra were calculated from the raw measurement data. The processed acoustic data were then further analyzed in MATLAB.

The MATLAB post-processing was based on TUM LLS processing tools previously developed for flight-test-based UAV noise analysis [4], [5]. For the present study, these tools were adapted and applied to the PW.Orca measurement campaign in order to prepare synchronized acoustic-flight datasets for the subsequent model analysis.

The first essential step in post-processing was the synchronization of the acoustic measurement data with the UAV flight-log data. This synchronization was performed using GPS timestamps available from both the measurement system and the UAV. Based on the synchronized UAV position and attitude data, source-receiver distances, emission angles and incidence angles at the microphone plates were calculated for all microphones.

After synchronization, propagation-time-delay and Doppler corrections were applied. Furthermore, a plate correction was applied, since the metallic ground plate beneath the microphones can influence different frequencies depending on the angle of incidence. In the next step, the pressure-doubling effect was corrected, since the microphones were positioned on acoustically hard metallic ground plates. Finally, A-weighted sound pressure levels, SPL(A), were calculated from the corrected acoustic data. Since the models developed in this work are intended to assess community-noise-related effects, A-weighted SPL was used as the target quantity for the semi-empirical models.

The resulting synchronized datasets formed the basis for the phase-specific source-model identification and for the subsequent analysis of wall-induced effects in the simplified urban flyover case.

4. Semi-Empirical Source Modeling Framework and Free-Field Results

4.1 General model philosophy and methodology

This section describes the framework used to develop phase-specific semi-empirical source models for the free-field UAV measurements. The approach is based on compact model formulations in which the model structure is defined using physically motivated input quantities. The free model parameters are identified from aeroacoustic measurements using an output-error parameter-identification approach following standard system-identification methodology [10]. For each phase, the model parameters were determined by minimizing the residual between measured and modelled A-weighted SPL over the selected time interval and microphones.

The modeling framework used in this study follows the semi-empirical point-source approach introduced in previous work [4], [5]. This approach provides the general basis for identifying compact source models from synchronized acoustic and flight-log data. In the present work, the framework is applied to the PW.Orca mission and adapted to the individual flight phases. This is motivated by the different propulsion and aerodynamic operating conditions occurring during hover-propeller-dominated vertical flight, transition and cruise. Previous experimental studies on multirotor vehicles have shown that hover and forward-flight conditions can exhibit different aeroacoustic characteristics, including rotor-airframe interaction effects in hover and rotor-wake interaction effects in forward flight [11].

For the vertical-flight phases, model terms describing dependency on electrical power, polar directivity and source-receiver distance are used. For the transition phases, flight speed is additionally included. For the cruise phase, an extended model is used, including electrical power, azimuthal and polar directivity, bank angle, flight speed, source-receiver distance and a background term. The general model structure can be written as

$$L_A = \mathrm{f}(P_{el}, \theta_{pol}, \varphi_{az}, r, V, \mu; \boldsymbol{p}) \tag{1}$$

where P_{el} is the electrical power, θ_{pol} and φ_{az} are the polar and azimuthal emission angles, r is the distance between the UAV and the microphone, V is the flight speed, μ is the bank angle and $\boldsymbol{p}$ is the vector of free model parameters. Not all variables are used in all flight phases. The specific set of model terms is selected according to the physical characteristics of the corresponding flight phase and the quality of the available data.

Based on the synchronized UAV position and attitude data, the source-receiver distance and emission angles are computed for each microphone and time step. These quantities form the geometric input variables of the semi-empirical models. All phase-specific models in this work were identified and evaluated using A-weighted sound pressure levels. This ensures consistency between the phase-specific models and provides the basis for a later mission-level application. For the identification of the free-field source models, only the six field microphones listed in Table 1 were used. Wall-side microphones were excluded from source-model identification and are later used to evaluate the urban/wall extension in the simplified urban flyover case.

The flight-phase segmentation was derived from the synchronized UAV flight-log data and was not based on the acoustic levels. The main indicators used for the segmentation were the recorded flight state, ground speed, electrical power, altitude trend, and the rotational speeds of the hover and cruise propellers. The vertical-flight phases were identified as flight segments with dominant hover-propeller operation and a continuous change in altitude. The transition and retransition phases were identified as intervals in which the UAV changed between hover- and cruise-propeller-dominated operation, together with acceleration or deceleration. The cruise phase was identified as the forward-flight segment with a quasi-steady flight-speed plateau and cruise-propeller-dominated operation. Table 1 summarizes the flight phases considered in this work and the microphones used for the corresponding model identification.

Phase	Microphones	Target
Vertical take-off	2, 3, 4, 6, 7, 8	L_A
Transition into cruise	2, 3, 4, 6, 7, 8	L_A
Cruise	2, 3, 4, 6, 7, 8	L_A
Retransition into landing	2, 3, 4, 6, 7, 8	L_A
Vertical landing	2, 3, 4, 6, 7, 8	L_A

Table 1 – Overview of the flight phases and field microphones used for the phase-specific source-model identification, L_A denotes A-weighted SPL.

For each phase, the model parameters were identified by minimizing the residual between measured and modelled A-weighted SPL over the selected time interval and microphones. The agreement between measured and modelled SPL was quantified using the root mean square error (RMSE)

$$\mathrm{RMSE} = \sqrt{\frac{1}{N}\sum_{i=1}^{N}(L_{A,meas,i} - L_{A,model,i})^2} \tag{2}$$

The reported RMSE values describe the agreement between the identified phase-specific model structures and the selected measurement segments. The identified model parameters are listed in Appendix A. The following subsections present the phase-specific model formulations and the corresponding free-field model results for one representative free-field microphone, Mic3, while the RMSE values are calculated over all field microphones.

4.2 Vertical-Flight Models

The vertical take-off and vertical landing phases are dominated by the hover propellers and are therefore modelled separately. The models include a propulsion-power-related term, since higher propeller power is expected to result in higher noise levels, a geometrical spreading term, since the sound pressure level decreases with increasing source-receiver distance, and polar directivity terms, since the UAV noise emission is directional and the emission angle relative to the microphone changes during the UAV motion.

During the take-off and landing phases, the UAV motion is dominated by the change of altitude. Therefore, the source-receiver distance and the polar emission angle change during vertical motion. Although the UAV altitude is not used as an explicit model input, it affects the model through these geometric quantities.

$$\begin{aligned} L_{A,hov} = {} & p_1 \log_{10}(P_{el}) + p_2 \sin(\theta_{pol} - p_3) + p_4 \cos(\theta_{pol} - p_5) \\ & - 20\log_{10}(r/40) \end{aligned} \tag{3}$$

The model result for the vertical take-off phase is shown in Figure 3. In addition to the time-domain comparison, the same model output is also plotted as a function of the UAV altitude relative to the beginning of the vertical-flight segment.

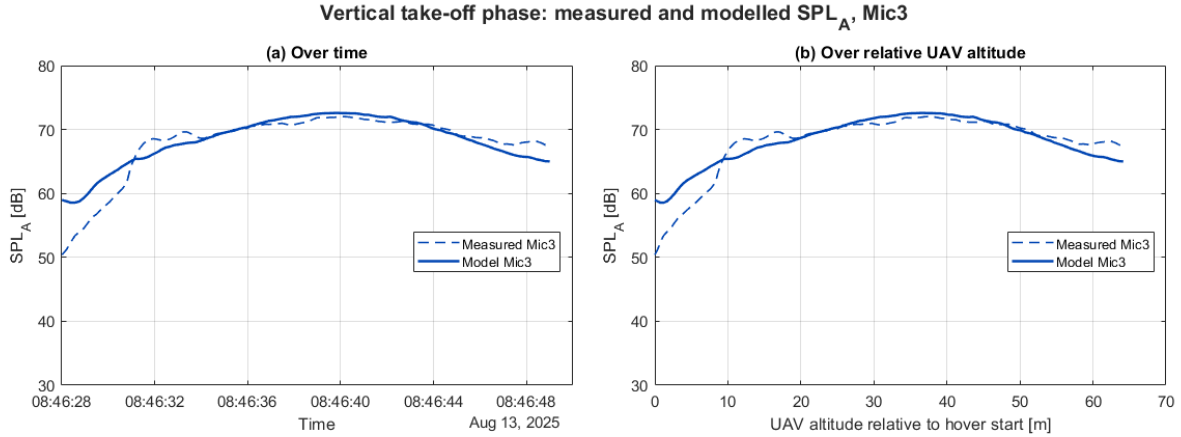


Figure 3 – Comparison between the measured data and the semi-empirical model results over time and relative UAV altitude change for the take-off phase.

For the landing case, the same model structure as for the take-off phase was used, but the parameters were identified separately using the data segment corresponding to the vertical landing phase of the mission. Figure 4 shows the comparison between the semi-empirical model and the measured data for the vertical landing case over time and as a function of the UAV altitude change relative to the beginning of the landing segment.

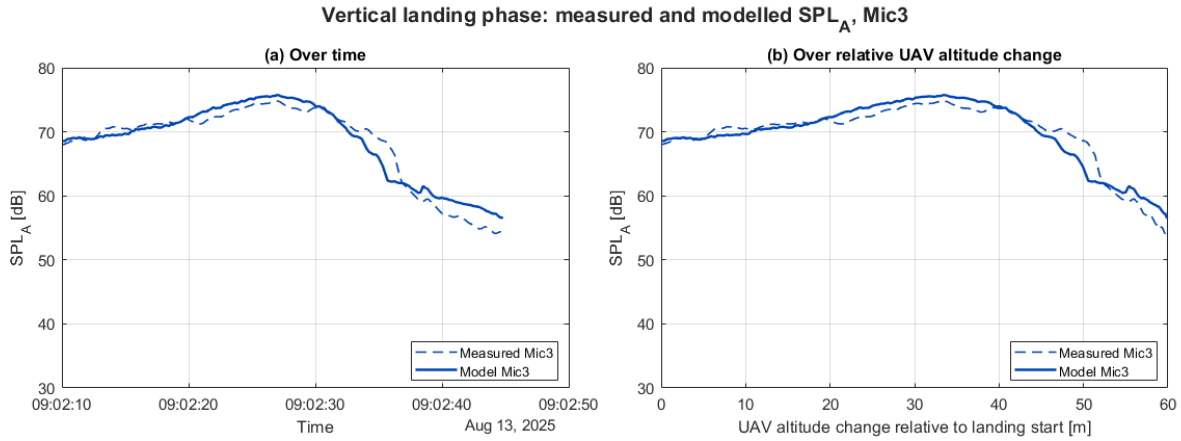


Figure 4 – Comparison between the measured data and the semi-empirical model results over time and relative UAV altitude change for the landing phase.

Table 2 shows the comparison between the take-off and landing models.

Phase	Main inputs	RMSE, dB(A)
Vertical Take-Off	P_{el}, θ_{pol}, r	1.79
Vertical Landing	P_{el}, θ_{pol}, r	2.08

Table 2 – Comparison of the vertical-flight models.

4.3 Transition Phase Models

The transition phase of the Orca represents the transition from vertical take-off into horizontal cruise flight, while the retransition phase represents the transition from cruise flight into vertical landing. During these phases, power is redistributed between the hover and cruise propellers, and the aerodynamic operating condition of the UAV changes continuously. For this reason, transition and retransition are treated as separate flight conditions and are modelled separately from the vertical-flight and cruise phases. The transition and retransition intervals were selected according to the phase segmentation described in Section 4.1.

An initial hypothesis for the transition phases was to represent the acoustic level as an energetic blending of the vertical-flight and cruise source models. This would imply that the transition noise can be described as a weighted combination of two quasi-stationary operating conditions. Two simple blending approaches were tested. In the first approach, the model was blended linearly in time, starting as a pure vertical-flight model at the beginning of the transition and ending as a pure cruise model at the end. In the RPM-based blend, the vertical-flight weight was calculated as the ratio of the average hover-propeller RPM to the sum of the average hover- and cruise-propeller RPM. Both gave clearly larger errors than the dedicated transition model, with RMSE values of 4.25 dB(A) and 4.18 dB(A), respectively, compared to 2.43 dB(A) for the dedicated transition model. Therefore, a simple weighted combination of the vertical-flight and cruise models was not retained for the final transition modeling.

Based on this result, the transition and retransition phases were modelled as separate flight phases. The transition model follows the compact vertical-flight-model structure but additionally includes flight speed as a transition-specific input variable. This accounts for the increasing forward-flight component during the transition into cruise.

$$L_{A,tr} = p_1 \log_{10}(P_{el}) + p_2 \sin(\theta_{pol} - p_3) + p_4 \cos(\theta_{pol} - p_5) - 20\log_{10}(r/40) + p_6 V \quad (4)$$

Figure 5 shows the comparison between the model and the measured data for the transition phase,

both over time and as a function of flight speed.

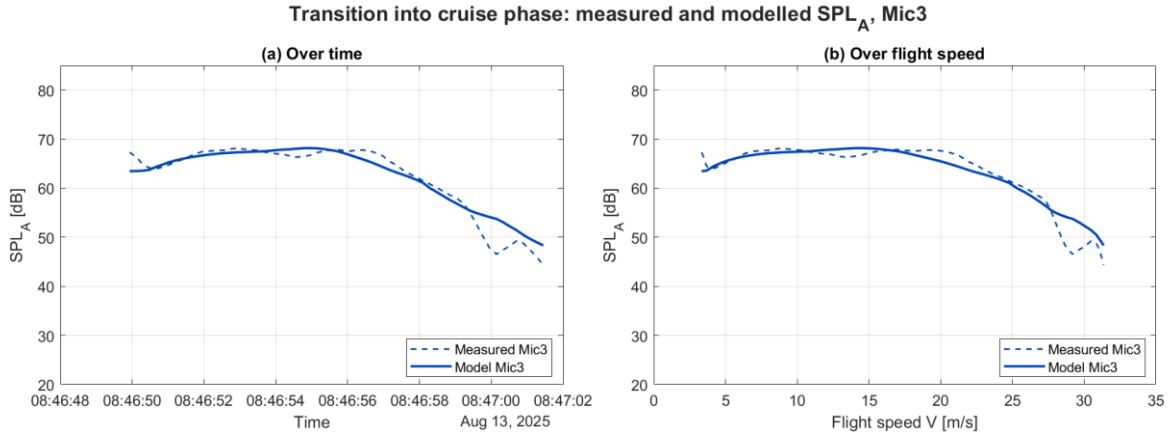


Figure 5 – Comparison between measured data and the transition into cruise phase model, shown over time and as a function of flight speed.

For the retransition into vertical landing, the same model structure was used. Figure 6 shows the comparison between the model result and the measured data for the retransition phase.

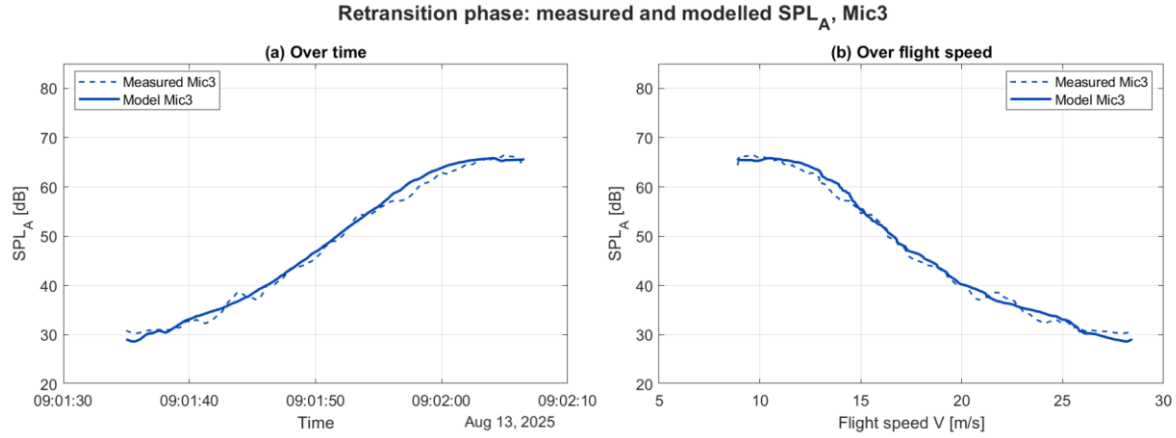


Figure 6 – Comparison between measured data and the retransition into vertical landing phase model, shown over time and as a function of flight speed.

Table 3 shows, similarly to the vertical-flight case, the comparison between the transition and retransition models based on the RMSE metric.

Phase	**Main inputs**	**RMSE, dB(A)**
Transition into cruise	P_{el}, θ_{pol}, r, V	2.43
Retransition into vertical landing	P_{el}, θ_{pol}, r, V	1.95

Table 3 – Comparison of the transition and retransition models.

4.4 Cruise Model

Cruise flight represents the most stationary flight phase of the UAV. In addition, it is the flight phase during which the UAV spends most of its operational time and therefore should be modelled as accurately as possible with respect to its impact on the community, while the vertical-flight and transition models presented in this work are kept compact.

The cruise model is formulated in two steps. First, the source-related contribution $L_{A,src}$ is calculated from the propulsion, directivity, attitude, distance and speed terms. Second, the broadband background term p_9 is added energetically to obtain the final cruise-model level $L_{A,cr}$:

$$L_{A,src} = p_1 \log_{10}(P_{el}) + p_2 \sin(\phi_{az} - p_3) + p_4 \sin(\theta_{pol} - p_5) + p_6 \cos(\mu) - p_7 \cdot 20\log_{10}\left(\frac{r}{40}\right) + p_8 V \tag{5}$$

$$L_{A,cr} = 10\log_{10}\left(10^{L_{A,src}/10} + 10^{p_9/10}\right)$$

In the source-related contribution $L_{A,src}$, the logarithmic power term accounts for the dependency of the noise emission on the electrical power demand of the propulsion system. The polar and azimuthal sinusoidal terms represent the directivity of the UAV noise emission. The distance term accounts for geometrical spreading relative to a reference distance of 40 m. The bank-angle term accounts for possible attitude-related variations during cruise flight. Finally, the speed term accounts for the influence of forward-flight velocity on the acoustic emission.

For the cruise-model evaluation, only selected straight flyover segments around the microphone array were considered. The selected segments cover the straight part of each cruise pass in the vicinity of the microphones, with a length of about 500 m, corresponding to roughly ±250 m around the microphone array. This selection excludes return-path portions of the circular mission, which are not representative of the selected straight flyover configuration around the microphone array. The first two cruise flyovers were additionally excluded because they were contaminated by noise from passing commercial aircraft.

Figure 7 shows the comparison between measured and modelled A-weighted SPL during cruise flight for a free-field Mic3 over two representative flyovers. The model reproduces the main flyover peak and the temporal development of the cruise passes with good agreement. This indicates that the selected set of input variables provides an adequate description of the broadband cruise noise level under free-field conditions.

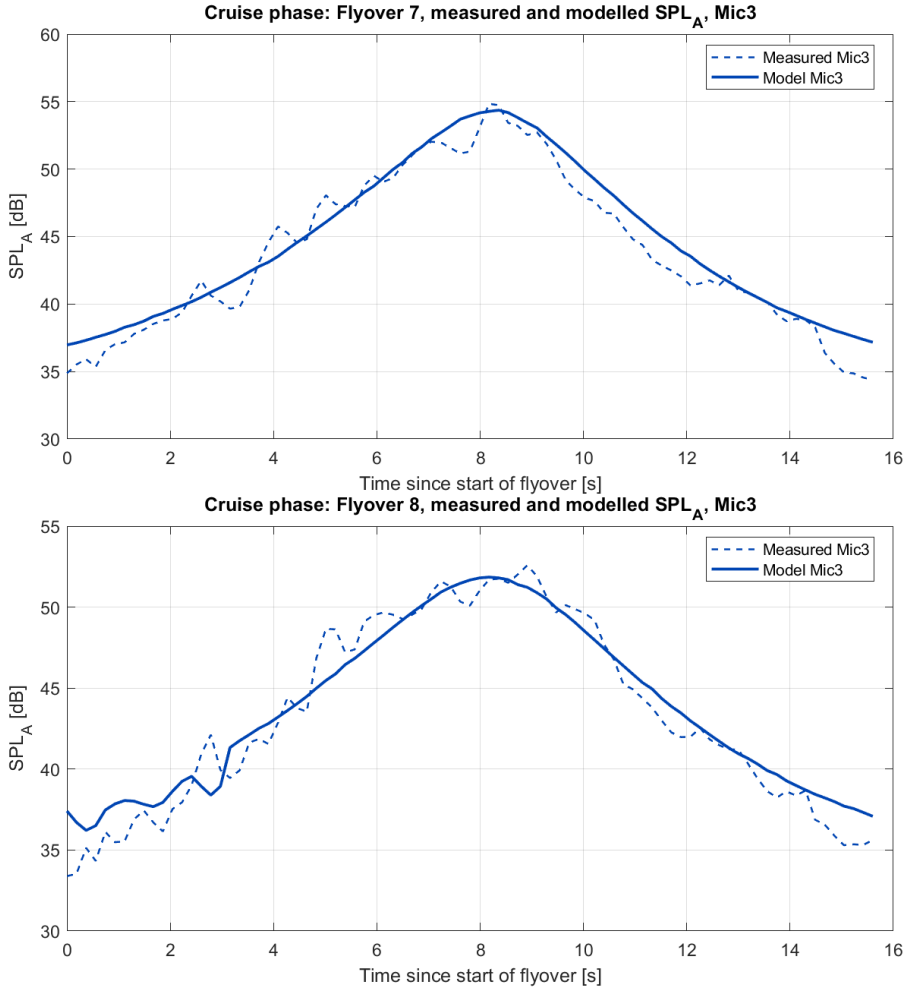


Figure 7 – Comparison between measured data and semi-empirical cruise-model results for two representative selected straight cruise flyovers at Mic3.

The RMSE reported in Table 4 was calculated over the remaining selected straight cruise flyover segments and all field microphones.

Phase	Main inputs	RMSE, dB(A)
Cruise	$P_{el}, \theta_{pol}, \phi_{az}, r, \mu, V$	1.685

Table 4 – RMSE of the cruise model.

Together with the vertical-flight and transition models presented above, the identified cruise model completes the set of phase-specific free-field source models considered in this work. The identified phase-specific models can be applied sequentially along a UAV mission timeline by selecting the corresponding model according to the flight-phase segmentation described in Section 4.1. In this way, the complete mission may be represented as a sequence of vertical take-off, transition into cruise, cruise, retransition into landing, and vertical landing segments.

5. Preliminary Extension to a Simplified Urban Flyover Case

This section describes the case of a simplified urban facade represented at the flight test field by a wall structure and investigates the possibility of extending the semi-empirical cruise model by testing a preliminary receiver-side image-source extension.

5.1 Experimental Setup

To account for a simplified urban environment, a wall structure with dimensions of 2.5 m × 2.5 m was installed at the flight test field. Two microphones were positioned in front of the wall at distances of 1 m and 2 m. However, the preliminary wall-model analysis presented here is restricted to Mic5 as one representative wall-side microphone. The remaining six microphones remained in the free field for comparison purposes. The objective of this setup was to measure the acoustic signal including wall-reflection effects and to investigate possible differences in the acoustic signature between free-field microphones and microphones positioned near the wall.

Since the objective of this work is to develop phase-specific semi-empirical UAV noise models, this setup is intended to provide a first step toward a receiver-side wall-extension for a simplified urban flyover case. The wall arrangement at the flight test field, as well as the two microphones positioned in front of the wall, are shown in Figure 8.



Figure 8 – Experimental setup at the flight test field for the simplified urban flyover case.

5.2 Wall-Effect Observation

The same processing steps described previously for the free-field data were also applied to the wall-measurement data. Figure 9 shows the measurement results of a single UAV mission recorded by one microphone in the free field (Mic4) and one microphone positioned near the wall (Mic5). To make both signals comparable despite the different microphone positions, the signals were time-shifted and

peak-aligned relative to the UAV trajectory.
The plot demonstrates a clear deviation between the free-field microphone measurement and the measurement near the wall. In particular, the shape of the flyover signature differs before and after the main peak. This deviation is observed consistently for each flyover and is therefore considered systematic.

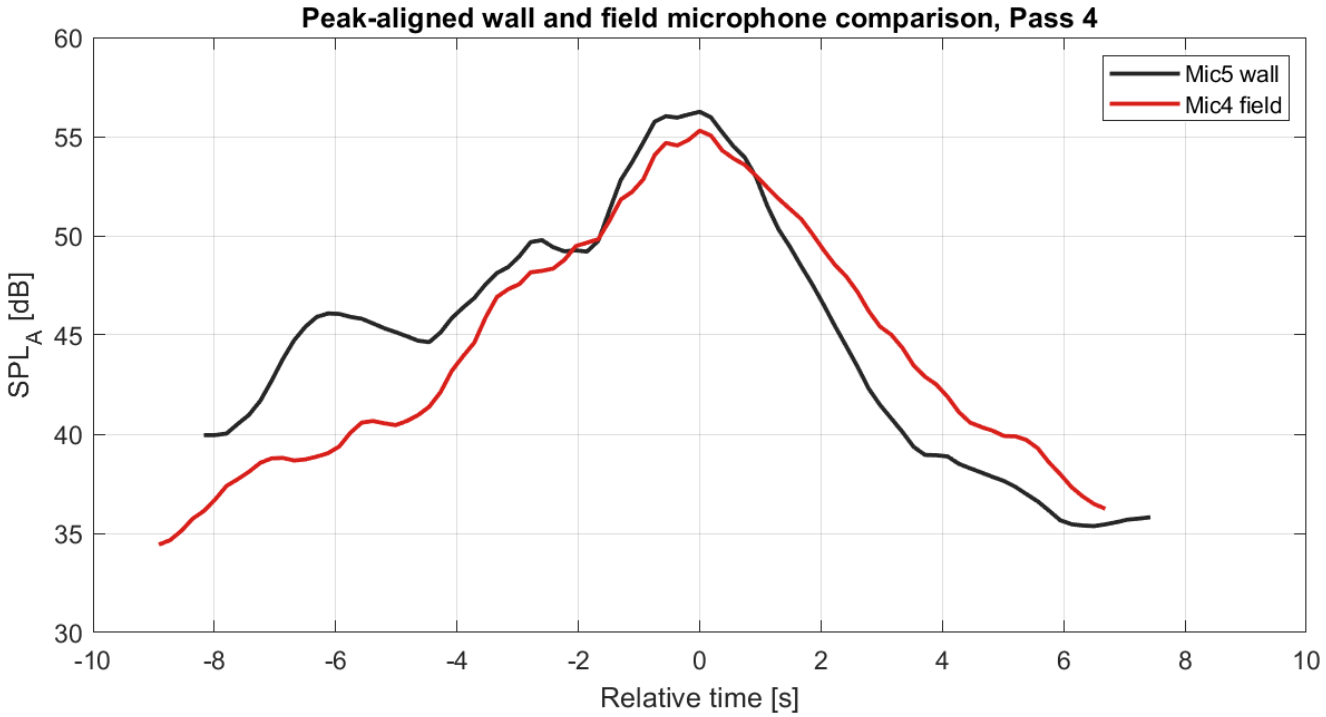


Figure 9 – Peak-aligned comparison of A-weighted SPL measured at a free-field microphone (Mic4) and a wall-side microphone (Mic5) for one representative UAV flyover.

5.3 Preliminary Wall-Model Extension

To assess the influence of the wall on the measured sound pressure level, the cruise flight phase was selected. In contrast to the free-field case, the wall-side microphone is affected not only by the direct sound emitted by the UAV, but also by additional propagation effects caused by the nearby reflecting surface.
As a first step, the free-field cruise model was applied to the wall-side microphone without re-identifying the source-model parameters. This allows the remaining deviations to be evaluated under the assumption that the UAV source model itself is already known, while the wall influence is initially neglected. This source-only approach underpredicts the wall-side measurement around the flyover peak and does not reproduce the characteristic temporal deviations before and after the peak. This indicates that the wall-side microphone response cannot be described by the free-field source model alone.
As a physically motivated first-order wall-extension, an image-source approach was considered [12]. In this approach, the reflected contribution is represented by a virtual source positioned symmetrically behind the wall plane. The image-source contribution is added energetically to the direct source prediction and scaled by a broadband reflection coefficient α:

$$L_{A,wall} = 10 \cdot \log_{10}(10^{L_{A,dir}/10} + \alpha \cdot 10^{L_{A,im}/10} + 10^{p_9/10}) \quad (6)$$

where $L_{A,dir}$ is the direct UAV source contribution evaluated with the cruise source formulation excluding the effective background term, $L_{A,im}$ is the corresponding mirrored image-source contribution, α is a broadband reflection coefficient and p_9 is the same broadband background term as used in the cruise model.
The image-source hypothesis was tested using the same selected straight cruise flyover segments as used for the cruise-model evaluation. For the idealized image-source case with α = 1, the predicted level is increased by approximately 2–3 dB and the agreement around the flyover peak is improved locally. However, the resulting curve does not reproduce the measured temporal structure before and

after the peak. Consequently, the RMSE over the selected straight wall-side flyovers increases from 2.81 dB(A) for the source-only model to 3.84 dB(A) for the ideal image-source case.
Since the idealized image-source case mainly improved the agreement around the flyover peak, the reflection coefficient was additionally fitted only in a small time window around the measured peak. For this purpose, a ±2 s window around the peak was selected. This local fit resulted in α = 0.58 and reduced the peak-window RMSE from 3.13 dB(A) for the source-only model to 2.44 dB(A) for the peak-fitted image-source model.
For Figure 10, both image-source cases are shown over the flyover together with the measured data and the source-only prediction. While the image-source contribution improves the agreement around the peak, neither fit reproduces the overall shape of the wall-side signal. In particular, the measured pre- and post-peak structure remains different from the image-source model curves.
These results indicate that the observed wall effect cannot be described as a uniform broadband level increase alone. Instead, the remaining deviations may be related to frequency-dependent interference, finite-wall geometry, edge diffraction and possible shielding effects. A more detailed wall-reflection model is therefore left for future work.

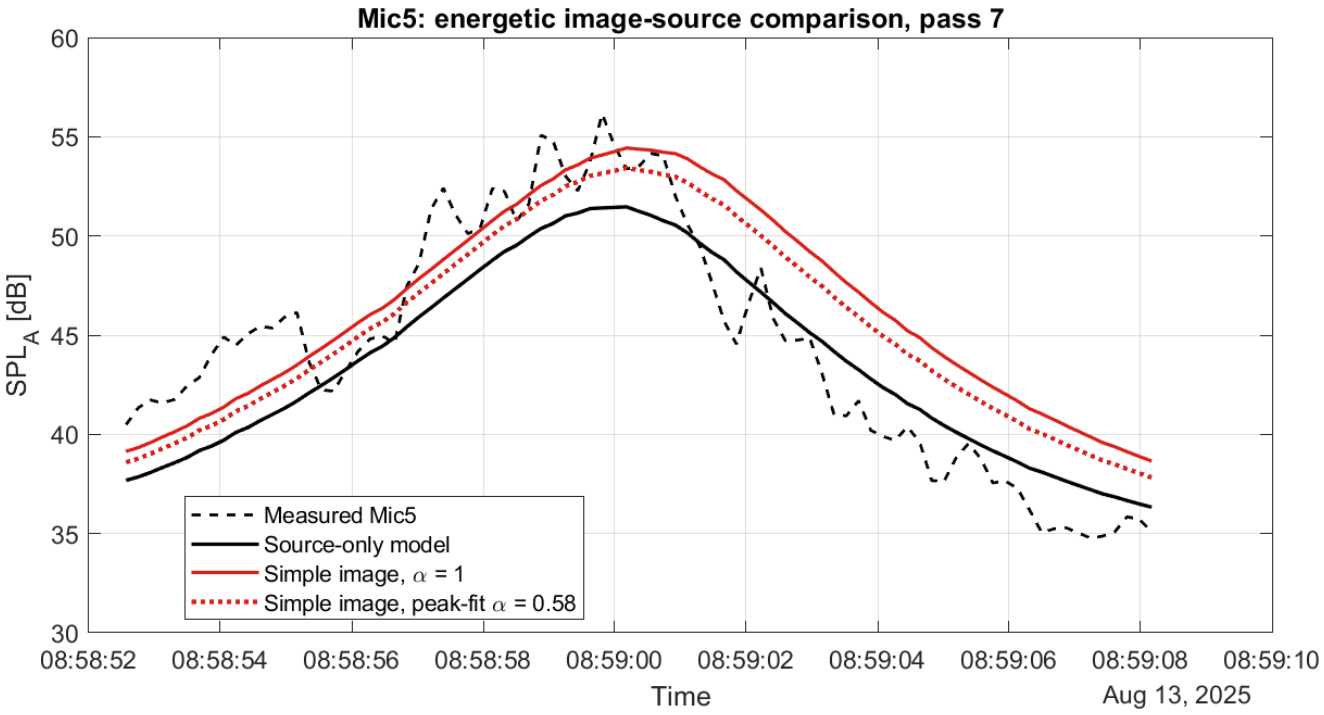


Figure 10 – Comparison between the wall-side measurement at Mic5, the source-only cruise model and two energetic image-source variants for one representative straight cruise flyover.

6. Discussion and Conclusion

In this work, phase-specific semi-empirical source models were developed for the PW.Orca cargo UAV with a separated lift and cruise configuration, based on synchronized acoustic and flight-log data. The results support the use of different model structures for the individual flight phases, as the underlying noise-generation mechanisms and operating conditions differ substantially between vertical-flight, transition and cruise.

The vertical take-off and landing phases could be described using compact vertical-flight models based on electrical power, polar directivity and source-receiver distance. For the transition and retransition phases, this compact structure was extended by flight speed. Simple vertical-flight/cruise blending approaches were tested for the transition phase but were not sufficient. Therefore, dedicated semi-empirical transition models were introduced. For the cruise phase, an extended model including electrical power, azimuthal and polar directivity, bank angle, flight speed, source-receiver distance and an effective background term was used. The cruise evaluation was restricted to selected straight flyover segments, while contaminated flyovers and return-path portions of the circular trajectory were excluded. All models were consistently identified using A-weighted acoustic data and physically motivated input quantities appropriate for the respective flight phase.

The phase-specific models provide a basis for a mission-level application of the modeling framework, where the corresponding model is selected according to the identified flight phase. Further flight missions are required as the next step to assess the transferability of the phase-specific modeling framework under different operating conditions and mission profiles.

In addition, the study investigated a preliminary receiver-side wall-extension for a simplified urban flyover case. The wall-side measurements showed systematic deviations from the free-field microphone measurements. Applying the source-only cruise model to the wall-side microphone reproduced the general flyover trend but did not capture the wall-side peak level and the temporal deviations before and after the peak. A simplified energetic image-source approach improved the agreement around the peak but did not reproduce the complete temporal structure of the wall-side signal. This indicates that a single broadband energetic image-source contribution is not sufficient to describe the observed wall-induced effects. A more detailed wall-reflection treatment is therefore required for future modeling of simplified urban flyover scenarios.

7. Outlook

Future work will focus on validating the phase-specific modeling framework on independent flight missions. This will make it possible to evaluate how well the identified models describe the noise emission of the UAV under different operating conditions and mission profiles.

For the simplified urban flyover case, additional measurements are planned to better understand wall-induced propagation effects. Future campaigns should include flyovers both perpendicular and parallel to the wall. On the modeling side, the wall extension should be developed toward a frequency- and geometry-dependent formulation including finite-wall visibility, coherent reflection, diffraction and possible shielding effects.

8. Acknowledgements

The authors would like to thank the Bavarian State Ministry for Economic Affairs, Regional Development and Energy for the sponsorship of the projects Environmentally Friendly and Safe eVTOL Transport in Urban Airspace (UmSiTrUL – Umweltfreundliche und sichere eVTOL Transporte im Urbanen Luftraum) and Environmentally Friendly Drone-Based Delivery Networks – Minimal Community Noise for Maximum Acceptance (MuteNet – Umweltfreundliche drohnengestützte Liefernetze – Minimaler Community Noise für maximale Akzeptanz), within which the presented results were obtained.

The authors also thank Prof. Schaller UmweltConsult GmbH and Phoenix-Wings GmbH for their cooperation and partnership within these projects.

9. Contact Author Email Address

To contact the author please use the following email address: illia.peleshok@tum.de

10. Copyright Issues

The authors confirm that they, and/or their company or organization, hold copyright on all of the original material included in this paper. The authors also confirm that they have obtained permission, from the copyright holder of any third party material included in this paper, to publish it as part of their paper. The authors confirm that they give permission, or have obtained permission from the copyright holder of this paper, for the publication and distribution of this paper as part of the ICAS proceedings or as individual off-prints from the proceedings.

References

[1] EASA, Study on the societal acceptance of Urban Air Mobility in Europe. European Union Aviation Safety Agency, 2021.

[2] Lotinga M. J. B., Ramos-Romero C., Green N., Torija A. J. Noise from Unconventional Aircraft: A Review of Current Measurement Techniques, Psychoacoustics, Metrics and Regulation. *Current Pollution Reports* 9:724–745, 2023. https://doi.org/10.1007/s40726-023-00285-4.

[3] Kawai C., Jäggi J., Georgiou F., Meister J., Pieren R., Schäffer B. Short-term noise annoyance towards drones and other transportation noise sources: A laboratory study. *Journal of the Acoustical Society of America* 156, 2578–2595, 2024. https://doi.org/10.1121/10.0032386.

[4] Speck S., Wilberg J. and Hornung M. An Approach for Aeroacoustic Footprint-Modeling of Low Altitude Platforms

by Means of Time Domain System Identification, 2013, *Aviation Technology, Integration, and Operations Conference*, Los Angeles, CA, 2013.

[5] Schmähl M., Rieger C., Speck S., Hornung M. Semi-empiric noise modeling of a Cargo eVTOL UAV by means of system identification from flight noise measurement data. *CEAS Aeronautical Journal* 13:85–96, 2022. https://doi.org/10.1007/s13272-021-00551-5.

[6] Wunderli J. M., Meister J., Boolakee O., Heutschi K. A Method to Measure and Model Acoustic Emissions of Multicopters. *International Journal of Environmental Research and Public Health* 20, 96, 2023. https://doi.org/10.3390/ijerph20010096.

[7] Schäfer P., Reich L., Vorländer M. Linking atmospheric and urban auralization models. *Acta Acustica* 6:28, 2022. https://doi.org/10.1051/aacus/2022021.

[8] Phoenix Wings GmbH.: https://phoenixwings.com/ [Online]. Available: https://phoenixwings.com/pworca/ Accessed 25 May 2026.

[9] EASA, Guidelines on Noise Measurement of Unmanned Aircraft Systems Lighter than 600 kg Operating in the Specific Category (Low and Medium Risk), 2023.

[10] Jategaonkar, R. *Flight Vehicle System Identification*. American Institute of Aeronautics and Astronautics, Inc. 1801 Alexander Bell Drive, Reston, VA 20191-4344 (2015). ISBN: 978-1-62410-278-3.

[11] Zawodny N. S., Pettingill N. A. Acoustic Wind Tunnel Measurements of a Quadcopter in Hover and Forward Flight Conditions. *International Congress and Exposition on Noise Control Engineering*, Chicago, IL, 2018. NASA Technical Reports Server, Document ID 20200002564.

[12] Vorländer M. *Auralization. Fundamentals of Acoustics, Modelling, Simulation, Algorithms and Acoustic Virtual Reality*. Springer Nature Switzerland AG, Cham. 2020. RWTHedition. ISBN-eBook: 978-3-030-51202-6.

Appendix A. Identified Model Parameters

Flight phase	Identified parameters								
	p_1	p_2	p_3	p_4	p_5	p_6	p_7	p_8	p_9
Vertical Take-Off	8.1777	-25.2288	0.7278	18.0073	1.8933	-	-	-	-
Transition into cruise	10.2601	-17.6936	0.7799	-15.9494	1.6747	0.1402	-	-	-
Cruise	14.4911	1.0534	0.4222	0.5927	0.6560	0.5389	1.5865	0.3680	32.9494
Retransition into vertical landing	3.0329	30.7925	2.9538	35.2633	-0.6581	0.3589	-	-	-
Vertical Landing	9.7404	-21.4187	0.6367	-16.5354	2.0277	-	-	-	-

Table A1 – Identified parameters of the phase-specific semi-empirical source models.